Pergamon

Int. J. Heat Mass Transfer. Vol. 39, No. 18, pp. 3767–3780, 1996

0017-9310/96 $15.00 + 0.00

PII: S0017-9310(96)00066-X

A vapor flow model for analysis of liquid-metal heat pipe startup from a frozen state

JEAN MICHEL TOURNIER and MOHAMED S. EL-GENK†

Institute for Space and Nuclear Power Studies/Department of Chemical and Nuclear Engineering, School of Engineering, The University of New Mexico, Albuquerque, NM 87131, U.S.A.

(*Received* 28 *November* 1995 *and in final form* 8 *February* 1996)

Abstract—A free-molecular, transition and continuum vapor flow model, based on the dusty gas model, is developed and incorporated in HPTAM, a two-dimensional heat pipe transient analysis model, to analyze the startup of a radiatively-cooled sodium heat pipe from a frozen state. The calculated wall temperatures at different times during the startup transient are in good agreement with measurements. Results showed that minimal sublimation and resolidification of sodium occurred in the early time of the transient, during which the vapor flow is free molecular. The melting of sodium in the wick occurred initially in the radial direction, then axially after the complete thaw of the evaporator section. Subsequent evaporation of liquid sodium caused the vapor flow in the evaporator to transition to the continuum regime. A continuum vapor flow front propagated axially toward the condenser, following the melt front in the wick region. The heat rejection capability of the heat pipe increased gradually as the continuum vapor flow front traveled along the condenser. Copyright © 1996 Elsevier Science Ltd.

INTRODUCTION

The startup of liquid-metal heat pipes from a frozen state involves several highly nonlinear and tightly coupled heat and mass transfer processes in the vapor, wick and wall regions. The most challenging tasks have been the modeling of the phase-change in the wick and the free-molecular and transition flow regimes of the vapor. Jang *et al.* [1] developed a pure-conduction heat capacity method to predict the phase-change in the wick, and modeled the continuum vapor flow regime using a one-dimensional transient compressible flow model. They used the transition temperature at a Knudsen number of 0.01 to characterize the axial location of the free-molecular flow front, and in this regime they neglected the heat and mass transfers at the frozen wick–vapor interface. Hence, the model does not mechanistically account for the progressive accumulation of vapor in the heat pipe core during startup.

Cao and Faghri [2] improved the model of Jang *et al.* [1] by using a pure conduction fixed-grid enthalpy method to handle the change-of-phase in the wick, and modeled the continuum vapor flow regime using the two-dimensional compressible Navier–Stokes equations. They described the rarefied vapor flow regime using a self-diffusion model. The two vapor flow regions were coupled with appropriate boundary conditions at the front defined by the transition temperature.

The thermal hydraulic response of heat pipes under transients (THROHPUT) code of Hall and Doster [3] and Hall *et al.* [4] incorporates liquid flow in the wick, hydrodynamically couples the liquid and vapor phases, and uses the dusty gas model to describe the various vapor flow regimes and the effect of non-condensible gas in the vapor core (air) during startup of a liquid-metal heat pipe from a frozen state. Their two-dimensional conservation equations were averaged over the radial direction to yield one-dimensional vapor and wick axial models. Melting and freezing processes in the wick were modeled using an approximate solution. Hall and Doster assumed that the liquid and solid phases existed in radial concentric layers, and assumed a parabolic radial temperature distribution in each layer. The coefficients in the assumed temperature profiles were determined by satisfying the temperature and heat flux boundary conditions, and by matching the layer average temperature with that computed in the axial model. The axial propagation of the melt front was modeled by combining the radial thaw model with a lumped-parameters axial treatment. Because the THROHPUT model is basically one-dimensional, it does not mechanistically deal with the change-of-phase of the working fluid, hence, its predictions are only approximate.

Owing to the complexity of the problem, it is desirable to use a unified approach for modeling the vapor flow in the heat pipe, and couple it to a two-dimensional phase-change model in the wick during the startup from a frozen state. Due to the very low vapor pressure, and the relatively high fusion temperature of liquid–metal working fluids, the vapor flow is initially free-molecular, when the working fluid is frozen in the wick. After the working fluid in the evaporator section is melted, rapid evaporation causes the vapor flow in the evaporator to become transitional, and eventually

† Author to whom correspondence should be addressed.

NOMENCLATURE

a	inside radius of pipe [m]
D	flow diffusivity coefficient [$m^2 s^{-1}$]
e	internal energy per unit mass [J kg^{-1}]
E	total energy per unit mass, $E = e + \|\mathbf{U}\|^2/2$ [J kg^{-1}]
$\mathbf{F}$	external force acting on molecules [N]
h	enthalpy per unit mass, $h = e + p/\rho$ [J kg^{-1}]
k	Boltzmann constant, $k = 1.3804 \times 10^{-23}$ [J K^{-1}]
k	thermal conductivity [W $m^{-1} K^{-1}$]
Kn	Knudsen number, $Kn = \lambda/(2a)$
m	molecular mass [kg]
$\dot{\bar{m}}$	evaporation/condensation/sublimation/resolidification mass flux [kg $m^{-2} s^{-1}$]
n	molecular density [molecules m^{-3}]
$\mathbf{N}$	outward unit vector normal to the surface
p	pressure [Pa]
$\mathbf{q}$	liquid mean filter velocity in wick [m s^{-1}]
$\mathbf{Q}$	conduction heat flux [W m^{-2}]
r	radial coordinate
R_{int}	radius of liquid–vapor/solid–vapor interface [m]
t	time [s]
T	temperature [K]
T_{fus}	working fluid fusion temperature [K]
T_{int}	wick-vapor interfacial temperature [K]
T_{tr}	transition temperature between vapor flow regimes [K]
$\mathbf{U}^V$	vapor velocity [m s^{-1}]
$\mathbf{u}^k$	mean velocity of molecules of species k [m s^{-1}]
$\bar{\mathbf{u}}$	mass average velocity of a mixture of gases [m s^{-1}]
$\bar{v}_a$	average molecular speed, equation (A22) [m s^{-1}]
$\mathbf{v}^k$	diffusion velocity of molecules of species k, $\mathbf{v}^k = \mathbf{u}^k - \bar{\mathbf{u}}$ [m s^{-1}]
z	axial coordinate
$\mathbf{Z}$	unit vector in the axial direction.

Greek symbols

$\bar{\alpha}_n$	coefficient which accounts for the nonuniform velocity profile in the vapor
γ	volume fraction of frozen fluid in voids of wick
$\mathbf{\Gamma}^k$	molecular flux of species k, $\mathbf{\Gamma}^k = n_k \mathbf{u}^k$ [molecules $m^{-2} s^{-1}$]
δ_{ij}	Kronecker delta, $\delta_{ij} = 1$ if $i = j$, $\delta_{ij} = 0$ otherwise
ε	volume porosity (void fraction) of wick
λ	molecular mean free path, equation (A1) [m]
μ	dynamic viscosity [kg $m^{-1} s^{-1}$]
$[\pi]$	pressure tensor [Pa]
ρ	density [kg m^{-3}]
σ	effective molecular diameter [m]
σ	surface tension of liquid [N m^{-1}]
$[\bar{\tau}]$	deviatoric component of pressure tensor, $\bar{\tau}_{ij} = \pi_{ij} + p_v \delta_{ij}$.

Subscript/superscript

d	wall molecules (dust)
g	vapor phase (gas)
L	liquid phase of working fluid
m	porous matrix
r	radial component
S	frozen (solid) phase of working fluid
sat	saturation vapor pressure
V	vapor phase of working fluid
z	axial component.

Operators/notations

div	divergence of vector, $\mathrm{div}(\mathbf{q}) = \frac{1}{r}\frac{\partial}{\partial r}(r q_r) + \frac{\partial q_z}{\partial z}$
Δ	Laplacian of scalar, $\Delta T = \mathrm{div}(\nabla T) = \frac{1}{r}\frac{\partial}{\partial r}\left(r\frac{\partial T}{\partial r}\right) + \frac{\partial}{\partial z}\left(\frac{\partial T}{\partial z}\right)$
$\mathbf{\Delta}$	Laplacian of vector, $\mathbf{\Delta}(\mathbf{q}) = \left[\Delta q_r - \frac{q_r}{r^2}, \Delta q_z\right]$
$\mathbf{q}$	vector, $[q_r, q_z]$
$\|\mathbf{q}\|$	norm of vector, $\|\mathbf{q}\| = \sqrt{q_r^2 + q_z^2}$
$\bullet$	scalar product of vectors
∇	gradient of scalar, $\nabla T = \left[\frac{\partial T}{\partial r}, \frac{\partial T}{\partial z}\right]$
$\bar{\nabla}$	gradient of vector operator, $\bar{\nabla}\mathbf{q}\mathbf{q} = \left[q_r\frac{\partial q_r}{\partial r} + q_z\frac{\partial q_r}{\partial z}, q_r\frac{\partial q_z}{\partial r} + q_z\frac{\partial q_z}{\partial z}\right]$.

continuum. As melting of the working fluid in the wick proceeds, the melt and the continuum vapor flow fronts travel axially toward the condenser. Eventually, the continuum vapor flow regime dominates after the thaw process of the working fluid is completed. Therefore, there is a need to mechanistically model the vapor flow in high-temperature heat pipes during the startup from a frozen state. Also, since the progression

of the continuum vapor flow front in the heat pipe is directly coupled to the progression of the melt front of working fluid in the wick, the latter must be accurately modeled. A two-dimensional transient model is needed to track the melt front during the startup of liquid-metal heat pipes. Also, this phase-change model needs to be coupled to the vapor region both at the solid–vapor and melt–vapor interfaces.

The objective of this paper is to develop a unified model for continuum and noncontinuum vapor flow regimes occurring during the startup of high-temperature heat pipes from a frozen state. This vapor model is coupled to the wick thaw and flow models in HPTAM to mechanistically describe the startup process. HPTAM is then used to investigate the startup of a radiatively-cooled sodium heat pipe from a frozen state, and the model predictions are compared with experimental data [5].

MODEL DESCRIPTION

HPTAM has been under development for a number of years at the Institute for Space and Nuclear Power Studies. The model was first developed to simulate the transient operation of fully-thawed low-temperature heat pipes [6], in which the vapor flow is always in the continuum regime. HPTAM divides the cylindrical heat pipe into wall, wick and vapor regions, solves the two-dimensional transient conduction equation in the wall, and employs the two-dimensional, compressible Navier–Stokes equations in the vapor region of low-temperature heat pipes. Recently, a two-dimensional freeze-and-thaw model was developed and incorporated into HPTAM for simulating the startup of low-temperature heat pipes from a frozen state [7]. The freeze-and-thaw model employs the volume-averaged homogeneous enthalpy method to predict the melt progression of the working fluid during startup [7]

$$\frac{\partial}{\partial t}[\varepsilon\gamma(\rho h)_s+\varepsilon(1-\gamma)(\rho h)_L+(1-\varepsilon)(\rho h)_m]+\operatorname{div}[(\rho h)_L\mathbf{q}]=\operatorname{div}[\bar{k}_{eff}\nabla T]. \quad (1)$$

The liquid flow, in a fully-saturated isotropic wick, is modeled using the Brinkman–Forchheimer-extended Darcy's continuity and momentum equations [7]

$$\varepsilon\frac{\partial\rho_L}{\partial t}+\operatorname{div}[\rho_L\mathbf{q}]=0 \quad (2)$$

$$\frac{\rho_L}{\varepsilon}\frac{\partial\mathbf{q}}{\partial t}+\frac{\rho_L}{\varepsilon^2}\bar{\nabla}\mathbf{q}\mathbf{q}=\rho_L\frac{\mathbf{F}}{m}-\nabla p_L-\frac{\mu_L\mathbf{q}}{K}-\frac{C}{\sqrt{K}}\rho_L|\mathbf{q}|\mathbf{q}+\frac{\mu_L}{\varepsilon}\Delta\mathbf{q}. \quad (3)$$

Expressions for the hydrodynamic and thermal properties of the wire-screened wick, such as volume porosity, ε, permeability K, inertia coefficient C, and effective axial and radial thermal conductivities can be found in ref. [7].

The rates of sublimation, resolidification, evaporation and condensation occurring at different stages of the startup transient at the wick–vapor interface are obtained from the kinetic theory of gases, assuming an accommodation coefficient of unity

$$\dot{\bar{m}}=\left(\frac{m}{2\pi kT_{int}}\right)^{1/2}[p_v-p_{sat}(T_{int})]. \quad (4)$$

The vapor and liquid–wick regions are hydrodynamically and thermally coupled at the liquid–vapor (L–V) interface. The radial momentum jump condition at the L–V interface is given as [6]

$$(p_L-p_v)+2\frac{\sigma}{R_c}+\left(\frac{1}{\varepsilon\rho_L}-\frac{1}{\rho_v}\right)\dot{\bar{m}}^2=0. \quad (5)$$

The radius of curvature of the liquid meniscus, R_c, is related to the volume of vapor in the interfacial pores of the wick [7, 8].

Model of vapor flows in high-temperature heat pipes

The different approaches being considered for modeling the vapor flow in high-temperature heat pipes were critically reviewed (see Appendix). An analysis was performed to determine the most suitable unified approach which is accurate over the full range of vapor pressures, extending from the free-molecular to the continuum flow regime. The three commonly used vapor models are: (a) the Poiseuille or continuum flow model, (b) the self-diffusion model, and (c) the first and second approximations of the dusty gas model (DGM). These models were compared with experimental data for gas flow in capillary tubes obtained by Knudsen [9]. Results showed that only the DGM can accurately predict the vapor flow rate over the entire range of pressures, from the free-molecular to the continuum flow regime. The failure of the Navier–Stokes and the self-diffusion models to accurately describe the noncontinuum vapor flow regimes stems from the fact that they do not fully account for the effect of molecule collisions with the wall, which predominate at low pressure. The DGM incorporates this effect through describing the gas flow as a two-species diffusion problem involving the gas molecules and giant molecules representing the wall. The wall molecules (or dust) are assumed motionless and uniformly-distributed, and are formally treated as one component of a binary gas mixture (see Appendix).

The vapor flow regimes during the startup of a liquid-metal heat pipe are classified as follows:

free-molecular flow $Kn > 1.0$;
transition flow $0.01 < Kn < 1.0$;
continuum flow $Kn < 0.01$.

Based on this classification, the transition temperatures between the vapor flow regimes can be deter-

mined (see Appendix). Basically, for a 20 mm-diameter water heat pipe, the vapor flow is always continuum, even during the startup from a frozen state (Fig. A1). For liquid-metal working fluids, however, the vapor flow remains in the free-molecular regime even after the working fluid is fully-thawed and its temperature exceeds its fusion temperature (Fig. A1).

The free-molecular and transition flow regimes occurring in high-temperature heat pipes are described herein using a one-dimensional transient model based on the second approximation of the dusty gas model for gas flow in a circular channel. The general forms of the mass, axial momentum, and energy conservation equations for a pure gas are obtained from the microscopic Boltzmann formulation [10]. When integrated over the vapor control volume depicted in Fig. 1(a), these equations can be written as

$$\iiint_{\mathrm{Vol}} \frac{\partial \rho_{\mathrm{V}}}{\partial t}\,\mathrm{d}V + \oiint_{\partial \mathrm{Vol}} \rho_{\mathrm{V}} \mathbf{U}^{\mathrm{V}} \bullet \mathbf{N}\,\mathrm{d}A = 0 \tag{6}$$

$$\iiint_{\mathrm{Vol}} \frac{\partial}{\partial t}(\rho_{\mathrm{V}} U_z^{\mathrm{V}})\,\mathrm{d}V + \oiint_{\partial \mathrm{Vol}} \rho_{\mathrm{V}} U_z^{\mathrm{V}} (\mathbf{U}^{\mathrm{V}} \bullet \mathbf{N})\,\mathrm{d}A = \iiint_{\mathrm{Vol}} \rho_{\mathrm{V}} \frac{F_z}{m}\,\mathrm{d}V - \oiint_{\partial \mathrm{Vol}} p_{\mathrm{V}} \mathbf{Z} \bullet \mathbf{N}\,\mathrm{d}A + \oiint_{\partial \mathrm{Vol}} \bar{\tau}(\mathbf{Z}) \bullet \mathbf{N}\,\mathrm{d}A \tag{7}$$

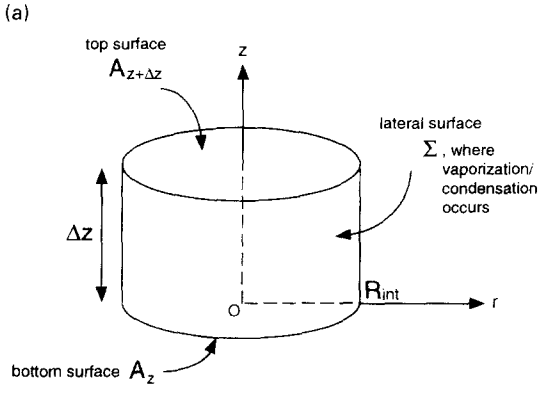

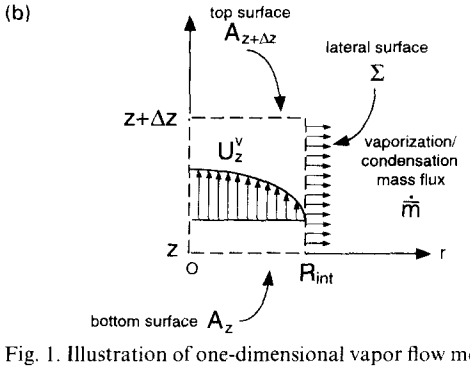

Fig. 1. Illustration of one-dimensional vapor flow model. (a) Vapor core control volume. (b) Vapor velocity profile.

$$\iiint_{\mathrm{Vol}} \frac{\partial}{\partial t}(\rho_{\mathrm{V}} E^{\mathrm{V}})\,\mathrm{d}V + \oiint_{\partial \mathrm{Vol}} \rho_{\mathrm{V}} E^{\mathrm{V}} (\mathbf{U}^{\mathrm{V}} \bullet \mathbf{N})\,\mathrm{d}A = \iiint_{\mathrm{Vol}} \rho_{\mathrm{V}} \mathbf{U}^{\mathrm{V}} \bullet \frac{\mathbf{F}}{m}\,\mathrm{d}V - \oiint_{\partial \mathrm{Vol}} \mathbf{Q}^{\mathrm{V}} \bullet \mathbf{N}\,\mathrm{d}A - \oiint_{\partial \mathrm{Vol}} p_{\mathrm{V}} \mathbf{U}^{\mathrm{V}} \bullet \mathbf{N}\,\mathrm{d}A + \oiint_{\partial \mathrm{Vol}} \bar{\tau}(\mathbf{N}) \bullet \mathbf{U}^{\mathrm{V}}\,\mathrm{d}A, \tag{8}$$

where ∂Vol, the surface of the control volume Vol, is the sum of the top, bottom and lateral surfaces. The areas of these surfaces are easily calculated: $A_z = A_{z+\Delta z} = \pi R_{\mathrm{int}}^2$, and $\Sigma = 2\pi R_{\mathrm{int}} \Delta z$. Also, $\mathrm{Vol} = A_z \Delta z$ [Fig. 1(a)]. The last term on the right-hand side of the energy conservation equation (8) represents the work of the viscous/diffusion forces acting on the surfaces of the control volume, and is neglected here; however, the energy dissipation in the volume is not neglected. As shown in Fig. 1(b), the axial vapor velocity profile is generally nonuniform over the cross section of the vapor core, a no-slip condition is assumed at the L–V and/or S–V interface, and the vaporization/condensation rate is assumed normal to the interface. In the limit, when Δz goes to zero, equations (6)–(8) reduce to the following one-dimensional local forms:

$$\frac{\partial \rho_{\mathrm{V}}}{\partial t} + \frac{\partial}{\partial z}(\rho_{\mathrm{V}} \bar{U}_z^{\mathrm{V}}) = -\frac{2}{R_{\mathrm{int}}} \dot{\bar{m}} \tag{9}$$

$$\frac{\partial}{\partial t}(\rho_{\mathrm{V}} \bar{U}_z^{\mathrm{V}}) + \bar{\alpha}_2 \frac{\partial}{\partial z}\left[\rho_{\mathrm{V}} (\bar{U}_z^{\mathrm{V}})^2\right] = \rho_{\mathrm{V}} \frac{F_z}{m} - \frac{\partial p_{\mathrm{V}}}{\partial z} + \frac{1}{\mathrm{Vol}} \oiint_{\partial \mathrm{Vol}} \bar{\tau}(\mathbf{Z}) \bullet \mathbf{N}\,\mathrm{d}A \tag{10}$$

$$\frac{\partial}{\partial t}\left\{\rho_{\mathrm{V}}\left[h^{\mathrm{V}} + \bar{\alpha}_2 \frac{1}{2}(\bar{U}_z^{\mathrm{V}})^2\right]\right\} + \frac{\partial}{\partial z}\left\{\rho_{\mathrm{V}} \bar{U}_z^{\mathrm{V}}\left[h^{\mathrm{V}} + \bar{\alpha}_3 \frac{1}{2}(\bar{U}_z^{\mathrm{V}})^2\right]\right\} = \frac{F_z}{m} \rho_{\mathrm{V}} \bar{U}_z^{\mathrm{V}} + \frac{\partial p_{\mathrm{V}}}{\partial t} - \frac{\partial Q_z^{\mathrm{V}}}{\partial z} - \frac{2}{R_{\mathrm{int}}}\left\{\dot{\bar{m}}\left[h^{\mathrm{V}} + \frac{1}{2}\left(\frac{\dot{\bar{m}}}{\rho_{\mathrm{V}}}\right)^2\right] + Q_r^{\mathrm{V}}\right\}_{R = R_{\mathrm{int}}}. \tag{11}$$

The coefficients $\bar{\alpha}_n$ in equations (10) and (11) account for the nonuniform axial velocity profile in the vapor and are defined by the following integral relations:

$$\iint_A (U_z^{\mathrm{V}})^n\,\mathrm{d}A = \bar{\alpha}_n (\bar{U}_z^{\mathrm{V}})^n, \tag{12}$$

for $n = 2$ and $n = 3$. By definition, $\bar{\alpha}_1$ is equal to 1, since $\bar{U}_z^{\mathrm{V}}$ is the cross-sectional average of vapor axial velocity. For a fully-developed laminar flow, $\bar{\alpha}_2 = 4/3$

and $\bar{\alpha}_3 = 2$. By contrast, $\bar{\alpha}_2 = 1.020$ and $\bar{\alpha}_3 = 1.058$ for a fully-developed turbulent flow. Clearly, the factors $\bar{\alpha}_2$ and $\bar{\alpha}_3$ are functions of the Knudsen number, Kn. However, for simplicity, these factors are assumed unity in the present calculations. As will be shown later, even though this approach could underpredict the advections of axial momentum and kinetic energy of vapor by a factor as much as 2, the numerical predictions compare very well with experimental data for the startup of a sodium heat pipe. This is because the advection of axial momentum is small compared to the pressure gradient and pressure losses, while the advection of kinetic energy is smaller than that of the enthalpy. In fact, the vapor in the heat pipe is nearly saturated.

The last term on the right-hand side of equation (10) represents the pressure losses per unit volume. Unfortunately, no general expression for $\bar{\tau}$ is available for the case of an arbitrary Knudsen number. To remedy this problem, the results of the second approximation of the dusty gas model are used to identify these pressure losses (see Appendix)

$$\frac{1}{\mathrm{Vol}} \oiint_{\partial \mathrm{Vol}} \bar{\tau}(\mathbf{Z}) \bullet \mathbf{N}\, \mathrm{d}A = \left[\frac{\partial p_{\mathrm{v}}}{\partial z}\right]_{\mathrm{losses}}^{\mathrm{DGM}} = -\frac{kT_{\mathrm{v}}}{m} \times \frac{\rho_{\mathrm{v}} \bar{U}_z^{\mathrm{v}}}{[D]_2^{\mathrm{DGM}}}. \quad (13)$$

Equations (1)–(3) and (9)–(11) are solved subject to the following boundary and initial conditions: (a) the liquid and vapor velocities equal zero at all solid boundaries of the numerical domain (nonslip condition); (b) both ends of the heat pipe are insulated; (c) isoflux, adiabatic and radiative boundary conditions are applied independently at the wall in the evaporator, adiabatic and condenser sections, respectively; and (d) initially, the vapor, solid and wall temperatures are uniform and equal; the vapor pressure equals the saturation pressure of the working fluid, and the radius of the S–V interface, R_{int}, is uniform and equal to that of the screen/wick surface.

NUMERICAL SOLUTION

The finite-difference discretization method used to solve the governing equations in the wall, wick and vapor regions is based on the SIMPLEC segregated iterative solution technique; it is described in details in refs. [7, 11]. An efficient, iterative strongly-implicit solver (SIS) is used to solve the five-point momentum and enthalpy systems of equations, while the Gauss-elimination solver is used to solve the elliptic Poisson equation. A banded version of this solver was developed, which significantly reduced the amount of memory storage and CPU time [11]. The numerical scheme used in HPTAM is inherently stable, and can handle melting of pure metals and eutectics at discrete temperatures by using a phase-change temperature range for the mushy region as small as 10^{-8} K (limited only by machine accuracy). This numerical scheme does not require under-relaxation of the temperature; more details can be found in refs. [7, 11].

BENCHMARK OF MODEL

The ability of HPTAM to model the operation of fully-thawed heat pipes has been successfully demonstrated using experimental data for a water heat pipe [6]. The freeze-and-thaw model in HPTAM has been verified through comparisons with analytical solutions for the pure conduction one-dimensional Neumann problem and the two-dimensional problem of freezing in a corner, and experimental data on the freezing of pure tin in a rectangular enclosure in the presence of natural convection [7].

Due to the idealized initial conditions and the absence of consistent data on the startup of water heat pipes from a frozen state, it was not possible to test the freeze-and-thaw model using actual heat pipe experimental data. Some of the difficulties stem from the fact that in the experiment the distribution of ice in the wick is not well documented. The simulated results of the startup of a water heat pipe from frozen state [7], however, were consistent with reported experimental observations [12] that: (a) it is difficult to prevent dryout of the evaporator wick due to depletion of ice in this region by sublimation in the early stage of startup, followed by evaporation in the absence of significant liquid return until the ice in the condenser is melted; (b) during the early stage of startup, sublimation and resolidification processes are effective transport mechanisms for depleting the ice in the evaporator and accumulating it in the condenser section; (c) the reduction in volume upon melting of ice in the wick also contributes to the occurrence of early dryout in the evaporator.

The thaw process of high-temperature heat pipes is quite different, due to the fundamental differences in thermophysical properties, such as: (a) decrease of working fluid density upon melting; (b) negligible mass transport by sublimation/resolidification due to the significantly lower vapor pressure; and (c) in the early stage of startup, the vapor transport in high-temperature heat pipes is basically by free-molecular and transition flows. As will be seen later, these differences make it possible to start up a high-temperature heat pipe from a frozen state without encountering a dryout in the evaporator wick.

SIMULATION OF STARTUP OF A SODIUM HEAT PIPE FROM A FROZEN STATE

The transient vapor flow model described in the previous section is integrated into HPTAM and coupled to the wick thaw model for numerically simulating the startup of a high-temperature heat pipe from the frozen state. Results are compared with the experimental data of Faghri *et al.* [5] for a radiatively-

cooled sodium heat pipe. They employed a stainless steel (304L) heat pipe, 962 mm long, 22.4 mm i.d., with a wall thickness of 2.15 mm. In the evaporator, the heat pipe had four independently-controlled, Inconel-600 flexible electrical heaters, each 53 mm-wide, separated by 90 mm-long adiabatic sections. The fourth heater and the condenser were separated by a 188 mm-long transport section. Both the evaporator and transport sections were insulated with concentric radiation heat shields to minimize radiation losses, and fitted with water-cooled calorimeters to measure the actual heat losses. Heat was removed from the 292 mm-long condenser section by radiation to a water-cooled double-walled copper calorimeter. The measured emissivity of the condenser was 0.645. The circumferential wick of the heat pipe was made up of two wraps of 100-in^{-1} mesh stainless-steel screen, which had a wire diameter of 114 μm, an effective pore radius of 70 μm, and a porosity $\varepsilon = 0.70$. Assuming a clearance of 32.7%, the porous wick could have been 0.666 mm thick [7]. The heat pipe was tested in a vacuum chamber at an ambient temperature of 290 K, with a sodium charge of 30.0 grams.

The present calculations simulate the startup in the experiments number (11a)–(11d) of Faghri *et al.* [5], in which only the heater number 1, the one closest to the evaporator end cap, was active. At startup, the electrical power to the heater was maintained at a constant level of 311 W. At steady state, the measured heat losses to the water-cooled calorimeters were 161, 12 and 119 W in the evaporator, adiabatic and condenser sections, respectively. This means that 52% of the electrical power input to the heater was lost by radiation in the evaporator section.

To simulate the startup experiment number (11a), the effective lengths of the evaporator, adiabatic and condenser sections were taken as 53, 617 and 292 mm, respectively. These sections were discretized into 3, 35 and 16 axial cells, respectively. In the radial direction, 1, 3 and 9 cells were used to represent the vapor, porous wick and wall regions. The evaporator was heated uniformly at a power level of 119 W. An exponential period of 50 s was used to account for the thermal inertia of the heater, radiation shields and the calorimeter structures. Also, the wall thickness (4.3 mm) was taken equal to twice the actual pipe wall thickness in the experiment to account for the thermal inertia of and losses to the heat pipe's mounting assembly and inactive heaters. The transition temperatures corresponding to $Kn = 0.01$ and $Kn = 1.00$, and a vapor core diameter of 21.07 mm are 686 K and 540 K, respectively (Appendix, Fig. A1).

Radial melting of working fluid in the evaporator wick

Initially, the working fluid in the wick is frozen at a uniform temperature of 290 K. The startup is initiated by heating the evaporator with an exponential period of 50 s to 119 W (Fig. 2). After about 2 min into the transient, the working fluid at the evaporator wall begins to melt, with the melting front propagating

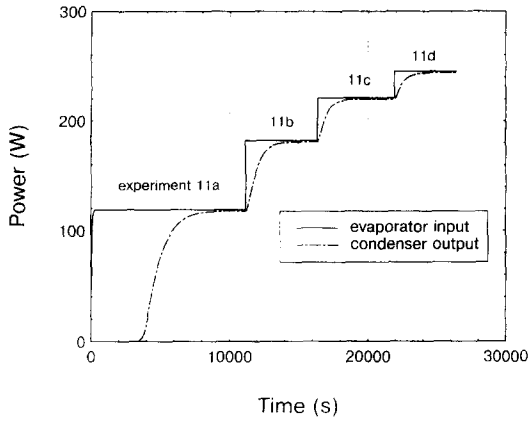

Fig. 2. Calculated evaporator input and condenser output powers during startup of the sodium heat pipe.

radially inward [Fig. 3(a)]. Although sublimation and resolidification occur at the S–V interface, only a negligible amount of the working fluid was transported by sublimation to the condenser, owing to its very low vapor pressure. Complete melting of the working fluid in the evaporator occurred very rapidly, in less than 1 min, because the wick is very thin (0.666 mm), and the heat capacity and heat of fusion of sodium are relatively low, only about one third of that of water.

After the working fluid in the evaporator was completely melted, working fluid evaporation occurred at the L–V interface, whereas the vapor flow was still rarefied or free-molecular. As evaporation continued, the mass of vapor in the evaporator core increased [Fig. 3(b)]. After about 8 min into the transient, continuum flow was established along the evaporator section, at which time the vapor temperature reached roughly the transition temperature of 686 K. The remaining length of the heat pipe was still in the free-molecular flow regime [Fig. 3(c)].

Axial propagation of continuum vapor flow front in the adiabatic section

After the working fluid in the evaporator wick was fully thawed, the melting and the continuum vapor flow fronts propagated axially toward the condenser [Fig. 3(d)]. It took about 50 min for these fronts to traverse the 617 mm-long adiabatic section of the heat pipe, at an average velocity of about 12 mm min^{-1}. Most of the heat input is utilized in the vaporization of the working fluid in the evaporator section. The startup behavior of this radiatively-cooled sodium heat pipe is characterized by a sharp dropoff in vapor and wick temperatures, corresponding to the transition vapor flow regime [Fig. 4(a)], and no vapor pressure recovery in the condenser [Fig. 4(b)]. During this period of startup, the heat pipe can be divided into several axial sequential zones [Fig. 3(d)]. In region (I), the evaporator, the vapor is in the continuum flow regime and evaporation occurs uniformly along the L–V interface [Fig. 4(c)]. This uniform mass injection into the vapor region causes the vapor velocity to

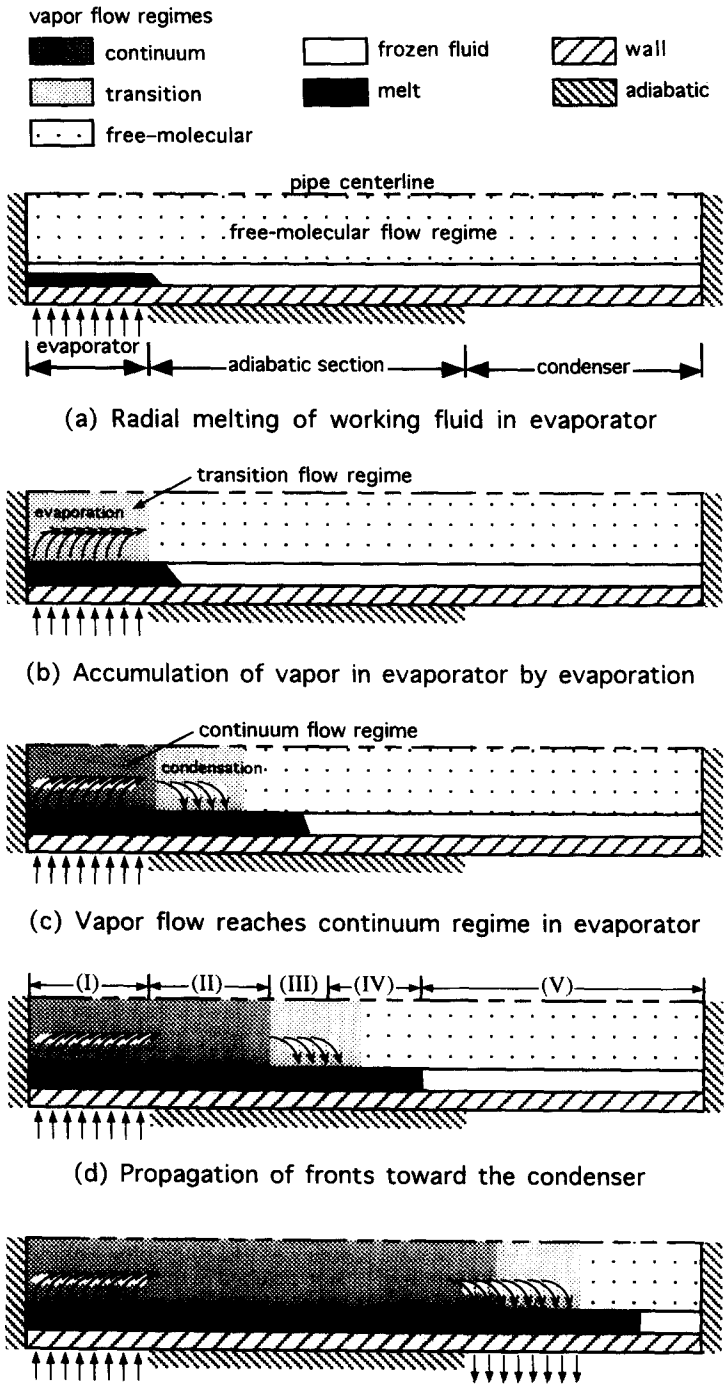

Fig. 3. Illustration of the startup of a radiative-cooled high-temperature heat pipe from a frozen state.

increase linearly along the evaporator [Fig. 4(d)]. In region (II), the vapor is in the continuum flow regime, and only minimal condensation occurs at the L–V interface. The vapor flow accelerates, however, due to the slow decreases in vapor temperature and density.

In region (III), the vapor pressure and temperature decrease rapidly, as the vapor flow changes to the transition regime [Fig. 4(a, b)]. In order for the continuum vapor flow front to move forward toward the condenser, heat must be supplied to increase the temperatures of the wick and the wall in the preceeding transition flow region. This is achieved by the condensation of vapor in this region [Figs. 3(d) and 4(c)]. Even though much vapor is removed by condensation, the vapor flow keeps accelerating due to the faster drops in vapor temperature and density.

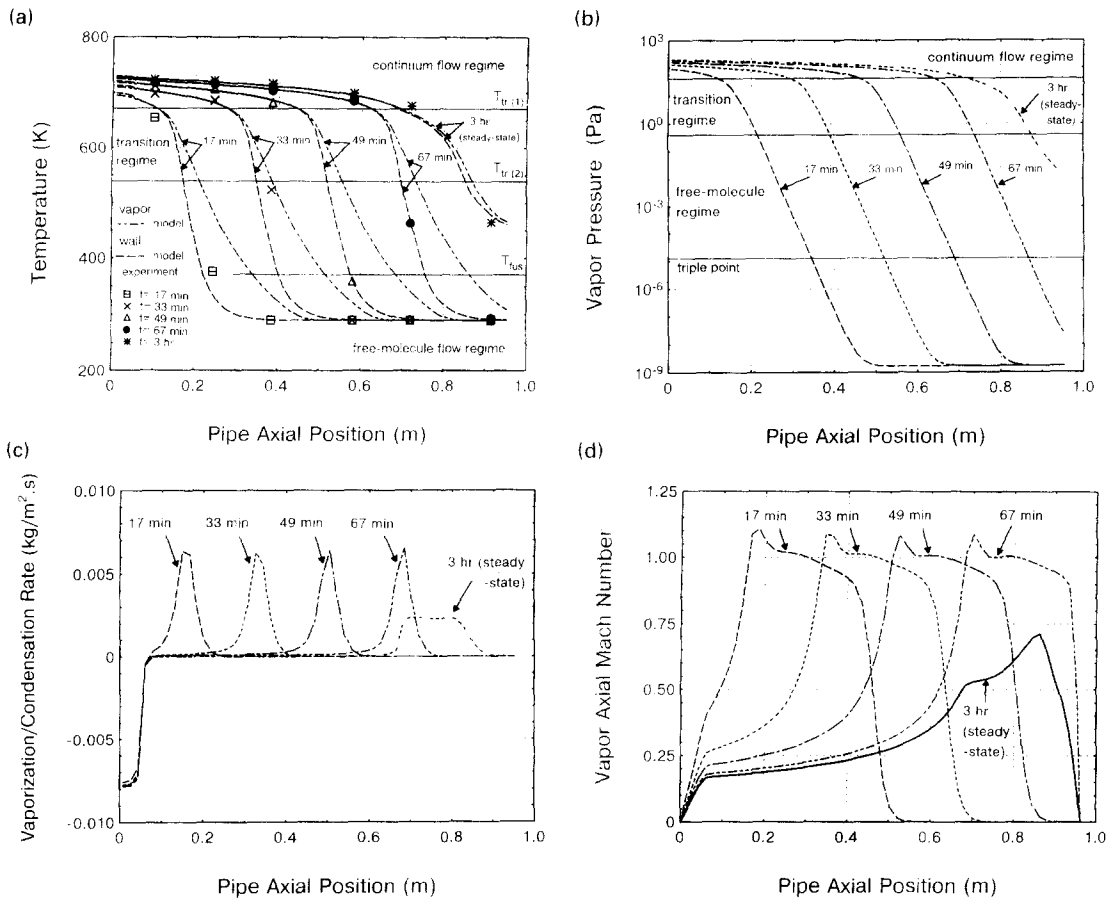

Fig. 4. Results of axial distributions at different times during startup experiment (11a). (a) Calculated and measured wall and vapor temperatures. (b) Calculated vapor pressure. (c) Calculated vaporization/condensation rates. (d) Calculated vapor axial Mach number.

The vapor Mach number reaches a value of 1 as the condensation rate peaks, at a vapor velocity of 630 m s^{-1} [Fig. 4(d)]. In region (IV) of the heat pipe, which is in the transition flow regime, the vapor velocity becomes slightly supersonic over a short distance, at a Mach number between 1 and 1.1, as the condensation rate drops quickly (the vapor pressure drops by two orders of magnitude).

Finally, in the frozen region (V), resolidification of vapor occurs at the S–V interface. However, only a minimal working fluid mass is involved in this process, since the axial vapor mass flow rate at the melting front is very small. The vapor axial velocity decreases steadily as resolidification proceeds along the frozen portion of the heat pipe. While the vapor velocity is subsonic in this region, it is still significant due to the very small density of the rarefied vapor [Fig. 4(d)]. The vapor pressure drops by seven orders of magnitude [Fig. 4(b)], and the vapor velocity drops abruptly to zero as the temperature difference between the vapor and the interface with the frozen wick vanishes [Figs. 4(a, d)]. The remaining portion of the frozen heat pipe remains completely inactive.

The wick in the evaporator remained saturated with liquid working fluid at all times during the startup transient. This is because sodium expands upon melting and little working fluid mass is lost by sublimation and resolidification in the frozen section of the heat pipe, owing to the very low vapor pressure of sodium. Indeed, the loss of working fluid by resolidification was more than compensated for by the volume expansion of the working fluid as the melting front propagated axially along the heat pipe. This volume expansion resulted in the formation of a liquid film in region (IV), which moved along, following the melting front.

Propagation of continuum vapor flow front in condenser

Once the continuum vapor flow front reaches the condenser section, the heat pipe begins radiating heat away [Figs. 2 and 3(e)], slowing down the propagation of the melt and the continuum vapor flow fronts. The heat pipe approaches steady state as the heat rejection rate in the condenser equates the net power input in the evaporator (Fig. 2, experiment 11a). At steady state, the working fluid in the wick is completely melted, but the portion at the far end of the condenser section remained in the transition and free-molecular flow regimes. This is because, at the present power throughout of 119 W, the active length of the condenser is determined by the surface area needed to

reject this heat load. At steady state, the condensation rate is uniform along the active length of the condenser section [Fig. 4(c)], and the vapor axial velocity is subsonic everywhere, with a maximum Mach number of 0.70 [Fig. 4(d)].

Faghri *et al.* [5] measured the outer wall temperature at six axial locations along the heat pipe. The wall thermocouples were located 100, 245, 385, 581, 720 and 915 mm from the outer edge of electrical heater number 1. As shown in Fig. 4(a), the calculated wall temperatures during the startup transient are in good agreement with the experimental data. Even though supersonic velocities occurred in the transport and condenser sections during the transient, the startup of the radiatively-cooled sodium heat pipe was not sonic limited. The capillary limit was not reached, and the startup of the sodium heat pipe from a frozen state was successful.

Modeling of experiments number (11*b*), (11*c*) *and* (11*d*) *of Faghri* et al. [5]

After 3 h, steady-state operation was reached in experiment (11a) (Fig. 2). Subsequently in experiments (11b)–(11d), the electrical power to the heater number 1 was increased stepwise to 182, 221 and 245 W, respectively. The transient response of the sodium heat pipe is shown in Fig. 2. About 92 min after the evaporator input power was increased from 119 to 182 W, steady-state operation was reached in experiment (11b). The steady-state results of experiments (11a), (11b), (11c) and (11d) are shown in Fig. 5(a, b). Again, the calculated wall temperatures are in good agreement with the experimental data. The extent of the noncontinuum flow regimes in the condenser diminished as the input power to the evaporator increased.

After 272 min, steady-state operation was reached in experiment (11b), whereas part of the condenser section was still in the free-molecular regime [Fig. 5(a, b)]. In experiment (11c), steady state was reached about 93 min later, at which time the entire length of the heat pipe was in the continuum flow regime, and the entire length of the condenser participated in the heat rejection process [Fig. 5(a, b)]. At steady state of experiments (11c) and (11d), the condensation rate was uniform along the entire length of the condenser section [Fig. 5(b)]. Figure 5(a) shows excellent agreement of the model predictions with measured wall temperatures along the heat pipe in experiments (11a)–(11d). This figure also shows mechanistically the progression of the various vapor flow regimes as the input power in the experiments was increased. Figure 5(b) clearly demonstrates that in the experiments (11a) and (11b), the condenser section did not fully participate in the heat rejection process. In experiments (11c) and (11d), however, the condenser participated in full. It was not until the power was increased to 245 W in experiment (11d) that the vapor flow along the entire length of the heat pipe became continuum.

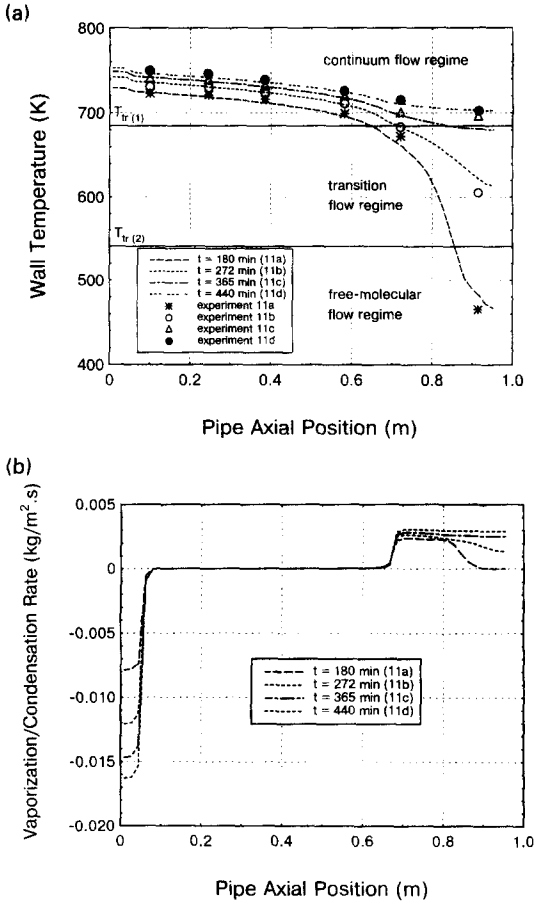

Fig. 5. Steady-state results of startup experiments (11a), (11b), (11c) and (11d). (a) Calculated and measured wall temperatures. (b) Calculated vaporization/condensation rates.

SUMMARY AND CONCLUSIONS

The capabilities of HPTAM, a two-dimensional heat pipe transient analysis model, were extended to include modeling of free-molecular and transition vapor flow regimes occurring during the startup of high-temperature heat pipes. The one-dimensional transient vapor flow model developed herein is based on the dusty gas model. The calculations were in good agreement with experimental data for the startup of a radiatively-cooled sodium heat pipe from a frozen state. Results showed that the startup of this heat pipe can be divided into three successive stages. During the first stage, the heat input is consumed in melting the working fluid in the evaporator wick. As soon as the working fluid in the evaporator is completely thawed, evaporation of working fluid occurs at the L–V interface. The accumulation of vapor in the evaporator region eventually raises the vapor pressure to the continuum flow regime. Subsequently, the melting front in the wick propagates axially toward the condenser, ahead of the continuum vapor flow front. During this stage and the previous one, the vapor flow in the condenser region is free-molecular and the condenser

is basically inactive. The arrival of the continuum vapor flow front to the condenser marks the beginning of the final stage of the startup, during which the rate of heat rejection gradually increases as the continuum vapor flow front travels through the condenser.

The heat pipe approaches steady state as the heat rejection rate in the condenser equals the input power in the evaporator, and the vapor flow throughout the heat pipe is in the continuum regime. The results indicated that when the radiatively-cooled sodium heat pipe of Faghri *et al.* [5] was operated at a relatively low input power of 119 W, the condenser only partially participated in the heat rejection at steady state, and the vapor flow at the far end (inactive) portion of the condenser was free-molecular. This flow transitioned to the continuum regime as the input power was increased to 245 W, and the condenser participated fully in the heat rejection process.

It is worth noting that in high-temperature liquid-metal heat pipes, the startup from a frozen state is easily attainable, without a partial dryout of the wick in the evaporator section; the wick remained saturated with liquid working fluid at all times during the startup. This is because liquid-metals expand upon melting and little working fluid mass is lost by sublimation and resolidification in the frozen section of the heat pipe, owing to the very low vapor pressures of liquid-metals.

Acknowledgements—This research is partially funded under NASA grant no. NAG3-941 and the University of New Mexico's Institute for Space and Nuclear Power Studies.

REFERENCES

1. J. H. Jang, A. Faghri, W. S. Chang and E. T. Mahefkey, Mathematical modeling and analysis of heat pipe startup from the frozen state, *ASME J. Heat Transfer* **112**, 586–594 (1990).
2. Y. Cao and A. Faghri, A numerical analysis of high-temperature heat pipe startup from the frozen state, *ASME J. Heat Transfer* **115**, 247–254 (1993).
3. M. L. Hall and J. M. Doster, A sensitivity study of the effects of evaporation/condensation accommodation coefficients on transient heat pipe modeling, *Int. J. Heat Mass Transfer* **33**, 465–481 (1990).
4. M. L. Hall, M. A. Merrigan and R. S. Reid, Status report on the THROHPUT transient heat pipe modeling code, in *Proceedings of the Eleventh Symposium on Space Nuclear Power and Propulsion*, Albuquerque, NM, 9–13 January, 1994, AIP Conference Proceedings no. 301 (Edited by M. S. El-Genk), Vol. 2, pp. 965–970 (1994).
5. A Faghri, M. Buchko and Y. Cao, A study of high temperature heat pipes with multiple heat sources and sinks, Part 1: Experimental methodology and frozen startup profiles, *ASME J. Heat Transfer* **113**, 1003–1009 (1991).
6. J.-M. Tournier and M. S. El-Genk, A heat pipe transient analysis model, *Int. J. Heat Mass Transfer* **37**, 753–762 (1994).
7. J.-M. Tournier and M. S. El-Genk, Transient analysis of the startup of a water heat pipe from a frozen state, *Numer. Heat Transfer A Applic.* **28**, 461–486 (1995).
8. J. T. Seo and M. S. El-Genk, A transient model for liquid-metal heat pipes. In *Space Nuclear Power Systems 1988* (Edited by M. S. El-Genk and M. D. Hoover), Vol. IX, pp. 405–418. Orbit, Malabar, FL (1989).
9. L. B. Loeb, *The Kinetic Theory of Gases*, pp. 290–300. McGraw-Hill, New York (1934).
10. J. O. Hirschfelder, C. F. Curtiss and R. B. Bird, *Molecular Theory of Gases and Liquids*, Chaps 7 and 8. Wiley, New York (1954).
11. J.-M. Tournier and M. S. El-Genk, A segregated solution technique for simulating the transient operation of heat pipes, *Numer. Heat Transfer B* **25**, 331–355 (1994).
12. J. M. Ochterbeck and G. P. Peterson, Freeze/thaw characteristics of a copper/water heat pipe: effects of non-condensible gas charge, *AIAA J. Thermophys. Heat Transfer* **7**, 127–132 (1993).
13. R. E. Cunningham and R. J. J. Williams, *Diffusion in Gases and Porous Media*, Chaps 1–3. Plenum Press, New York (1980).
14. M. S. El-Genk and J.-M. Tournier, A critical review of free-molecular and transition flow regimes in heat pipes, *Proceedings of the Ninth International Heat Pipe Conference*, Albuquerque, NM, 1–5 May, 1995 (Edited by M. A. Merrigan), Los Alamos National Laboratory, Los Alamos, NM (1995).
15. R. B. Evans III, G. M. Watson and E. A. Mason, Gaseous diffusion in porous media—II. Effect of pressure gradients, *J. Chem. Phys.* **36**, 1894–1902 (1962).
16. E. A. Mason, A. P. Malinauskas and R. B. Evans III, Flow and diffusion of gases in porous media, *J. Chem. Phys.* **46**, 3199–3216 (1967).

APPENDIX
VAPOR FLOW REGIMES IN HIGH-TEMPERATURE HEAT PIPES

During the startup of high-temperature heat pipes, the vapor pressure of working fluid is typically on the order of μPa. Hence, the mean free path of vapor molecules is large compared to the pipe diameter, and the vapor transport is by the *free-molecular flow*, which is limited by the molecule collisions with the wall. At temperatures several 100 K above the fusion temperature of the working fluid, the vapor pressure becomes large enough for the vapor flow to transition to the *viscous or continuum flow regime*. In this regime, characterized by a very small mean free path compared to the diameter of the pipe, the mass and momentum transfers are dominated by the molecule–molecule collisions. In the intermediate *transition flow regime*, both effects, molecule–molecule and molecule–wall collisions, are important. The transitions between these flow regimes can be characterized based on the value of Kn; the transition from continuum flow to transition flow typically occurs at $Kn = 0.01$, while that from transition flow to free-molecular flow occurs at $Kn = 1$. Figure A1 gives an estimate of these transition tem-

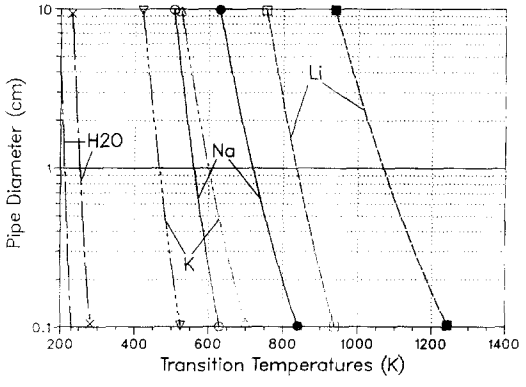

Fig. A1. Vapor flow chart for water and liquid-metal working fluids.

peratures as a function of heat pipe diameter. Assuming that molecules are nonattracting and behave as small hard spheres of diameter σ, Maxwell derived the following expression for the molecules mean free path [13]:

$$\lambda = \frac{1}{\sqrt{2}\pi\sigma^2}\frac{m}{\rho_V}, \tag{A1}$$

where the vapor density is that of the saturated phase. The transition temperature, T_{tr}, corresponding to a given value of Kn and a pipe diameter D, is then given as

$$D = 2a = \frac{\lambda}{Kn} = \frac{1}{Kn}\frac{k}{\sqrt{2}\pi\sigma^2}\frac{T_{tr}}{p_{sat}(T_{tr})}. \tag{A2}$$

In Fig. A1, the effective molecular diameter σ is taken as 2.8, 4.44, 3.58 and 3.0 Å for water, potassium, sodium and lithium, respectively. Figure A1 shows that for a liquid-metal heat pipe with a vapor core diameter of 20 mm, the transition temperatures from free-molecular to transition, and from transition to continuum flow are, respectively, 810 and 1030 K for lithium, 540 and 680 K for sodium and 450 and 570 K for potassium. These fluids are frozen at room temperature and their melting temperatures (453.7, 371.0 and 336.4 K, respectively) are well below their free-molecular transition temperature. The continuum flow regime exists in a liquid-metal heat pipe only at high temperatures. For a water heat pipe, however, the transition temperatures are quite low, due to the high vapor pressure of water (Fig. A1); viscous or continuum flow conditions prevail over the whole ranges of temperatures and pipe diameters of interest (micro-heat pipes are not included here).

VAPOR FLOW MODELS

The transport equations for a mixture of N gaseous components can be obtained from the summational invariants moments of the Boltzmann equations associated with each component and by combining them according to the form of the macroscopic properties of the mixture [10, 14]. The macroscopic formulation provides $(N+4)$ equations for the densities of species, n_k (or ρ_k), the mass average velocity of the mixture, $\vec{u}$, and the mixture temperature T (or internal energy, e). In order to mathematically close and solve this system of $(N+4)$ equations, constitutive relations for the pressure tensor $[\pi]$, the energy flux $\mathbf{Q}$, and the molecular fluxes of species Γ^k (or diffusion velocities for species $\mathbf{v}^k$) are needed. These quantities are complex integrals of the distribution functions and can be expressed in terms of the macroscopic quantities of the gas (n_k, $\vec{u}$ and T) using the solution of Grad and Zhdanov [10, 14].

Navier–Stokes, or continuum flow model

For a single component, the system of multicomponent equations reduces to the conservation equations and constitutive relations for a pure gas, in which the pressure tensor $[\pi]$ and heat flux vector $\mathbf{Q}$ are given by the constitutive relations of the Navier–Stokes–Fourier fluid model. The Navier–Stokes–Fourier equations, however, are only valid in the continuum regime. In the free-molecular and/or transition vapor flow regimes, where the effect of molecule–wall collisions becomes important or dominant, the viscous treatment of Navier–Stokes is inadequate.

Free-molecular and transition flow regimes

The kinetic theory of multicomponent systems gives the molecular flux of species (k) as

$$\Gamma^k = n_k\mathbf{u}^k = n_k(\vec{u}+\mathbf{v}^k) = \frac{n_k}{n}\Gamma_{vis}+\Gamma^k_{diff}, \tag{A3}$$

where $\Gamma_{vis} = n\vec{u}$, is the nonsegregative viscous molecular flux of the mixture, and $\Gamma^k_{diff} = n_k\mathbf{v}^k$, is the molecular diffusion flux of species (k). In the binary system of molecules A and B, when the thermal diffusion is negligible, the molecular diffusion flux of species A can be expressed as:

$$\Gamma^A_{diff} = n_A\mathbf{v}^A = -\frac{n^2}{\rho}m_B D_{AB}\mathbf{d}^A, \tag{A4}$$

where

$$\mathbf{d}^A = \nabla\left(\frac{n_A}{n}\right)+\left(\frac{n_A}{n}-\frac{\rho_A}{\rho}\right)\nabla\ln(p)-\frac{1}{p}\frac{\rho_A\rho_B}{\rho}\left[\frac{\mathbf{F}^A}{m_A}-\frac{\mathbf{F}^B}{m_B}\right]. \tag{A5}$$

In equation (A4), the binary diffusion coefficient, D_{AB}, needs to be evaluated. The first approximation of this (symmetric) coefficient, at low pressures, is given as [10, 14]

$$[D_{AB}]_1 = \frac{3}{8}\frac{1}{(n_A+n_B)}\frac{1}{\sqrt{2}}\left(\frac{1}{m_A}+\frac{1}{m_B}\right)^{1/2}\left(\frac{1}{\sigma_{AB}}\right)^2\left(\frac{kT}{\pi}\right)^{1/2} \times \frac{1}{\Omega^{(1,2)*}}. \tag{A6}$$

The molecular potential energy parameters characteristic of the interaction between molecules A and B, σ_{AB} and ε_{AB}, are usually obtained using the following empirical combining laws:

$$\sigma_{AB} = \frac{\sigma_A+\sigma_B}{2} \quad \text{and} \quad \varepsilon_{AB} = \sqrt{\varepsilon_A\varepsilon_B}. \tag{A7}$$

Equations (A4)–(A7) are the basis of the following models for describing the vapor flow.

Self-diffusion model

Some investigators have proposed using the self-diffusion model to simulate the free-molecular flow in heat pipes during startup [2]. In this model, for a binary gas mixture of species A and A^* having the same mass m_A and the same size and shape, $\sigma_{AA^*} = \sigma_A$ and $\varepsilon_{AA^*} = \varepsilon_A$, equation (A6) gives the self-diffusion coefficient as

$$[D_{AA^*}]_1 = \frac{3}{8}\frac{1}{(n_A+n_{A^*})}\frac{1}{\sqrt{m_A}}\left(\frac{1}{\sigma_A}\right)^2\left(\frac{kT}{\pi}\right)^{1/2}\frac{1}{\Omega^{(1,1)*}}. \tag{A8}$$

When the effects of pressure and thermal diffusions are neglected and the body forces are the only external forces acting on the gas molecules ($\mathbf{F}^k = m_k\mathbf{g}$), equation (A4) reduces to the well-known Fick's law of mass diffusion

$$\Gamma^A_{diff} = n_A\mathbf{v}^A = -n[D_{AA^*}]_1\nabla\left(\frac{n_A}{n}\right). \tag{A9}$$

For the particular case of interdiffusion of two different molecular species in a closed system, the viscous molecular flux in the mixture is null and the total molecular density n is constant, so that equation (A9) simplifies to

$$\Gamma^A = \Gamma^A_{diff} = n_A\mathbf{v}^A = -[D_{AA^*}]_1\nabla(n_A). \tag{A10}$$

By analogy with equation (A10), Cao and Faghri [2] used the following self-diffusion equation to simulate the free-molecular flow of vapor in the heat pipe during startup:

$$\Gamma = n\mathbf{u} = -[D_{AA^*}]_1\nabla(n). \tag{A11}$$

Dusty-gas-model (DGM)

The dusty gas model (DGM), introduced in the 1960s by Evans *et al.* [15] and improved later by Mason *et al.* [16], accounts for the effect of molecular collisions with the wall by simulating the latter as a collection of giant, uniformly-distributed dust molecules, which are stationary in the gas

flow. The governing equations are derived from the kinetic theory as a special case of multicomponent mixtures flow. In the governing equations of the DGM, the first component of the mixture, 'A', is the gas, represented by the letter 'g', and the second component 'B' is the wall molecules, or dust particles, referred to by the letter 'd'. The total densities and pressure in equations (A3) (A5) are given as

$$n = n_g + n_d, \quad \rho = \rho_g + \rho_d = m_g n_g + m_d n_d$$

$$\text{and} \quad p = p_g + p_d = n_g kT + n_d kT. \tag{A12}$$

Since the dust particles are uniformly distributed and stationary in space, their density, n_d, is constant, and the mixture mass average velocity and the gas mean velocity are related by $\rho\bar{\mathbf{u}} = \rho_g \mathbf{u}^g$. If a pressure gradient exists in the gas, a pressure diffusion term and a forced diffusion effect appear [equation (A5)]. The external force acts only on the dust particles, and arises from whatever clamping system the experimenter uses to keep the pipe wall stationary against the flow of gas. This external force can be expressed in terms of the gas pressure gradient [15] as

$$\mathbf{F}^d = \frac{1}{n_d} \nabla p_g. \tag{A13}$$

The introduction of equation (A13) into the expression for the molecular diffusion flux results in a considerable cancellation of terms [14], reducing equation (A5) to

$$\mathbf{d}^g = \frac{\nabla p_g}{p} - \frac{\rho_g}{\rho} \frac{n_d}{n} \frac{\nabla T}{T}. \tag{A14}$$

Since the dust particles are much larger than the gas molecules ($m_d \gg m_g$), the density of the mixture ρ is essentially that of the dust component ($\rho = \rho_g + \rho_d \approx \rho_d$). Thus by neglecting the thermal diffusion term, the molecular diffusive flux of the gas given by equation (A4) reduces to

$$\Gamma^g_{diff} = n_g \mathbf{v}^g = -\frac{n_g + n_d}{n_d} D_{gd} \left[\frac{\nabla p_g}{kT}\right]. \tag{A15}$$

The external force acting on the dust particles is obtained using Stokes' law for a sphere of diameter σ_d suspended in a moving fluid [16] as

$$\mathbf{F}^d = -(3\pi\sigma_d)\mu_g \bar{\mathbf{u}}. \tag{A16}$$

For a pure monoatomic gas, the Lennard–Jones spherical potential is adequate, and the dynamic viscosity can be expressed [10] as

$$\mu_g = \frac{5}{16\sigma^2}\sqrt{\frac{mkT_g}{\pi}} \times \frac{1}{\Omega^{(2,2)*}}. \tag{A17}$$

The function $\Omega^{(2,2)*}$, a collision integral which indicates the deviation of the Lennard–Jones molecular energy potential (of parameters σ and ε) from the idealized rigid-sphere model, is a tabulated function of the dimensionless temperature $T^* = kT/\varepsilon$. The viscous flux is thus given by

$$\Gamma_{vis} = n\bar{\mathbf{u}} = -\frac{n_g + n_d}{3\pi\sigma_d} \frac{\mathbf{F}^d}{\mu_g} = \frac{1}{(3\pi\sigma_d)} \frac{n_g + n_d}{n_d} \frac{\nabla p_g}{\mu_g}. \tag{A18}$$

Equation (A18) is analogous to Poiseuille's law for laminar flow through a pipe. Combining equations (A3), (A15) and (A18), and neglecting thermal diffusion, the total molecular flux is [14]

$$\Gamma^g = \frac{n_g}{n}\Gamma_{vis} + \Gamma^g_{diff} = -[D]^{DGM} \times \frac{\nabla p_g}{kT}. \tag{A19}$$

The total flow diffusivity in the dusty gas model, $[D]^{DGM}$, is the sum of two terms, the viscous and the Knudsen flow diffusivities, $[D]^{DGM} = [D]^{vis} + [D]^K$, where

$$[D]^{vis} = \frac{1}{(3\pi\sigma_d n_d)} \frac{p_g}{\mu_g} = \frac{A_d}{\mu_g} p_g = a^K p_g, \tag{A20}$$

and

$$[D]^K = \frac{n_g + n_d}{n_d} D_{gd}. \tag{A21}$$

The factor A_d in equation (A20) is a geometric constant characteristic of the dust particles only, so that the viscous flow diffusivity is proportional to the gas pressure. In order to apply the DGM model, an expression for the binary diffusion coefficient, D_{gd}, is needed.

First approximation of DGM binary diffusion coefficient, $[D_{gd}]_1$

Because the dust particles are much heavier ($m_d \gg m_g$) and much larger ($\sigma_d \gg \sigma_g$) than the gas molecules, the expression for $[D_{gd}]_1$, equation (A6), is greatly simplified. The collision integral also simplifies to $\Omega^{(1,2)*}_{gd} = 1 + S_{gd}$, where S_{gd} is a collision parameter depending on the angular scattering pattern between the gas and the wall molecules [14, 16]. Thus, the Chapman–Enskog first approximation of the Knudsen flow diffusivity of the DGM, which is independent of the gas pressure, can be written as

$$[D]^K_1 = \frac{3}{8} \frac{1}{n_d(\sigma_d)^2} \times \frac{1}{1 + S_{gd}} \left(\frac{8kT}{\pi m_g}\right)^{1/2} = B_{1d}\left(\frac{8kT}{\pi m_g}\right)^{1/2} = B_{1d}\bar{c}_a = b^K_1. \tag{A22}$$

where the factor B_{1d} is a geometric constant characteristic of the dust particles only.

Second approximation of DGM binary diffusion coefficient, $[D_{gd}]_2$

Using the Chapman–Enskog expression of $[D_{dg}]_2$, the Knudsen diffusivity of the DGM is [13, 16]

$$[D]^K_2 = b^K_2 \frac{1 + c^K_1 p_g}{1 + c^K_2 p_g}. \tag{A23}$$

where

$$b^K_2 = B_{2d}\bar{c}_a, \quad \frac{c^K_1}{c^K_2} = \frac{C_1}{C_2} = constant, \text{ and } \quad c^K_1 = C_1 \frac{a}{\mu_g}\left(\frac{m_g}{kT}\right)^{1/2}. \tag{A24}$$

The geometric constants A_d, B_{1d}, B_{2d}, C_1 and C_2 are functions of the dust particle parameters (n_d, m_d and σ_d) and can only be related to the macroscopic parameters of the geometry of interest (a and L) through specification of the boundary conditions. The proportionality constants can be evaluated from knowledge of the geometrical structure of the wall, using available experimental data and/or theoretical results at extreme values of the Knudsen number, namely, the Poiseuille and the Knudsen flow regimes. The average axial molecular flux of a gas [equation (A19)] in a pipe of radius a and length L can be expressed as

$$\bar{\Gamma}^g = -[D]\frac{1}{kT}\frac{dp_g}{dz}, \tag{A25}$$

where $[D]$ is the axial flow diffusivity. In the continuum flow regime, the DGM flow diffusivity is reduced essentially to the viscous flow diffusivity, $[D]^{vis}$. For a smooth pipe, the well-known Hagen–Poiseuille law [13] applies, and the viscous flow diffusivity has the form

$$[D]^{vis} = \frac{a^2}{8\mu_g} p_g, \tag{A26}$$

which identifies

$$A_d = \frac{a^2}{8} \quad \text{and} \quad a^K = \frac{a^2}{8\mu_g}. \tag{A27}$$

Similarly, at very low gas pressure ($Kn > 1$), the molecular density is so low that the molecules travel independently. For a long pipe of radius a, the fundamental relation deduced by Knudsen [13] for a free-molecular flow is

$$[D]^{Kn} = \frac{2}{3} a \bar{v}_a. \tag{A28}$$

This expression agrees well with free-molecular flow regime experiments [13]. In the free-molecular flow regime, the first and second approximations of the DGM flow diffusivity give the coefficients b_1^K and b_2^K, as

$$B_{1d} = B_{2d} = \frac{2}{3} a \quad \text{and} \quad b_1^K = b_2^K = \frac{2a}{3} \bar{v}_a. \tag{A29}$$

COMPARISON OF VAPOR FLOW MODELS

In this section, the three models described earlier for modeling the vapor (or gas) flow in the free-molecular, transition and continuum regimes are compared with experimental data for gas flow in capillary tubes [9]. As indicated earlier, the diffusivity for the continuum flow regime is proportional to the gas pressure, and is given by the well-known Hagen–Poiseuille law [equations (A26) and (A27)]

$$[D]^{vis} = a^K p_g, \quad \text{where} \quad a^K = \frac{a^2}{8\mu_g}. \tag{A30}$$

For the self-diffusion model, the flow diffusivity is equal to the self-diffusion coefficient, which is given by equation (A8) as

$$[D]^{self} = \left[\frac{3}{8} \frac{kT}{\sqrt{m_g}} \left(\frac{1}{\sigma_g}\right)^2 \left(\frac{kT}{\pi}\right)^{1/2} \times \frac{1}{\Omega^{(1,1)*}}\right] \frac{1}{p_g}. \tag{A31}$$

Note that this coefficient is inversely proportional to the gas pressure. The flow diffusivity for the first approximation of the DGM is given by equations (A19)–(A22) and (A29), as

$$[D]_1^{DGM} = [D]^{vis} + [D]_1^K = a^K p_g + b^K,$$

$$\text{where} \quad b^K = \frac{2a}{3} \bar{v}_a = \frac{2a}{3} \left(\frac{8kT}{\pi m_g}\right)^{1/2}. \tag{A32}$$

This coefficient is a linear function of the gas pressure. On the other hand, the flow diffusivity for the second approximation of the DGM is given by equations (A19)–(A24) and (A29), as

$$[D]_2^{DGM} = [D]^{vis} + [D]_2^K = a^K p_g + b_2^K \frac{1 + c_1^K p_g}{1 + c_2^K p_g},$$

$$\text{where} \quad c_1^K = C_1 \frac{a}{\mu_g} \left(\frac{m_g}{kT}\right)^{1/2} \quad \text{and} \quad \frac{c_1^K}{c_2^K} = \frac{C_1}{C_2}. \tag{A33}$$

In this equation, the two dimensionless constants C_1 and C_2 are determined from experiments [9]. Figure A2(a, b) shows some of Knudsen's data [9], in the form of a plot of the axial flow diffusivity [equation (A25)] as a function of the inverse of the Knudsen number, or gas pressure, for the flow of carbon dioxide at room temperature (25°C) through a bundle of 24 capillary tubes ($L = 20$ mm, $a = 33.3$ μm). The curve shows a minimum at $Kn = 1.2$, which characterizes the flow of gas in capillaries. The location of this minimum generally depends on the properties of the gas and the pipe dimensions. The semi-empirical expression proposed by Knudsen to describe such curves has the exact same form as equation (A33). By applying the method of least squares to his experimental results, Knudsen deduced that the ratio $C_1/C_2 = 0.81$. In fact, Knudsen's experiments bear out the fact that the ratio C_1/C_2 varies between 0.78 and 0.85 and is independent of the tube radius and the type of the gas [9]. A value of 0.81 agrees also with experimental results of other investigators, who found values ranging between 0.79 and 0.91 [13]. Therefore, there is a strong evidence that the ratio C_1/C_2 is a universal constant.

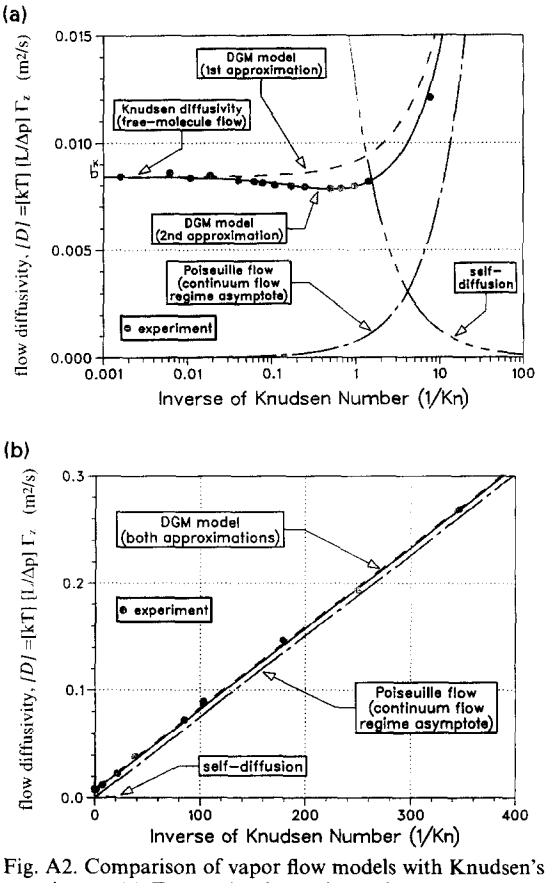

Fig. A2. Comparison of vapor flow models with Knudsen's experiment. (a) Free-molecular and transition regimes. (b) Continuum or viscous flow regime.

In this work, in the second approximation of the DGM, $C_1/C_2 = 0.81$ and $C_2 = 4$, which best fit the experimental data of Knudsen, were used. Also, $m_g = 7.305 \times 10^{-26}$ kg, $\sigma_g = 3.996 \times 10^{-10}$ m, and $\varepsilon_g/k = 190$ K [10], and a gas dynamic viscosity $\mu_g = 1.6 \times 10^{-5}$ kg m^{-1} s^{-1} [equation (A17)], were used.

The results of the various vapor flow models were compared with experimental data in Fig. A2(a, b). In the free-molecular flow regime, where the flow diffusivity is independent of pressure, both approximations of the DGM model predicted the data quite well. Because the Poiseuille model predicts no flow at such low pressure, it is not suitable

for this regime. As the gas pressure increased (or Knudsen number decreased), the flow began a progressive transition from the free-molecular to the viscous regime. The complete transition took place over roughly a two orders of magnitude change in gas pressure. The minimum in the flow diffusivity (in the transition flow region) is only predicted by the second approximation of the DGM. At high gas pressures, characteristic of the continuum flow regime ($Kn < 0.02$), the Knudsen diffusivity in equations (A32) and (A33) is negligible, while the viscous flow diffusivity increases proportional to the gas pressure. In this flow regime, the two DGM approximations are reduced essentially to the Poiseuille model [Fig. A2(b)]. As Fig. A2(a) shows, the self-diffusion model [equation (A31)] is not suitable for any flow regime. In an attempt to remedy this problem, Cao and Faghri [2] multiplied the self-diffusion diffusivity by an arbitrary factor $10^{(T/T_{tr})^{5}-1}$ when $T > T_{tr}$, where T_{tr} is the transition temperature given by equation (A2) with $Kn = 1$.